








**Please cite the Published Version**

Mei, Yu, Li, Yujin, Wang, Haoji, Gao, Jinqiang, Ni, Lianshan, Silvester, Debbie S , Banks, Craig E , Deng, Wentao, Chen, Baishan, Zou, Guoqiang, Hou, Hongshuai , Liu, Tongchao , Ji, Xiaobo , Liang, Chaoping  and Amine, Khalil  (2025) Tetrahedral Lithium Stuffing in Disordered Rocksalt Cathodes for High-Power-Density and Energy-Density Batteries. *Journal of the American Chemical Society*. ISSN 0002-7863

**DOI:** <https://doi.org/10.1021/jacs.4c15631>

**Publisher:** American Chemical Society (ACS)

**Version:** Accepted Version

**Downloaded from:** <https://e-space.mmu.ac.uk/638234/>

**Usage rights:**  [Creative Commons: Attribution 4.0](https://creativecommons.org/licenses/by/4.0/)

**Additional Information:** This is an author-produced version of the published paper. Uploaded in accordance with the University's Research Publications Policy

**Enquiries:**

If you have questions about this document, contact [openresearch@mmu.ac.uk](mailto:openresearch@mmu.ac.uk). Please include the URL of the record in e-space. If you believe that your, or a third party's rights have been compromised through this document please see our Take Down policy (available from <https://www.mmu.ac.uk/library/using-the-library/policies-and-guidelines>)

# Tetrahedral Lithium Stuffing in Disordered Rocksalt Cathodes for High-Power-Density and Energy-Density Batteries

Yu Mei, Yujin Li, Haoji Wang, Jinqiang Gao, Lianshan Ni, Debbie S. Silvester, Craig E. Banks, Wentao Deng, Baishan Chen, Guoqiang Zou, Hongshuai Hou, Tongchao Liu,\* Xiaobo Ji,\* Chaoping Liang,\* and Khalil Amine\*

Li-rich cation-disordered rocksalt (DRX) materials introduce new paradigms in the design of high-capacity Li-ion battery cathode materials. However, DRX materials show strikingly sluggish kinetics due to random Li percolation with poor rate performance. Here, we demonstrate that Li stuffing into the tetrahedral sites of the Mn-based rocksalt skeleton injects a novel tetrahedron-octahedron-tetrahedron diffusion path, which acts as a low-energy-barrier hub to facilitate high-speed Li transport. Moreover, the enhanced stability of lattice oxygen and the suppression of transition metal migration preserve the efficacy of the Li percolation network during cycling. Overall, the tetrahedral Li stuffing DRX material exhibits high energy density (311 mAh g<sup>-1</sup>, 923 Wh kg<sup>-1</sup>) and high-power density (251 mAh g<sup>-1</sup>, 697 Wh kg<sup>-1</sup> at 1000 mA g<sup>-1</sup>). Our results highlight the potential to develop high-performance and earth-abundant cathode materials within the extensive range of rocksalt compounds.

## 1. INTRODUCTION

The rapid expansion of lithium-based energy storage has highlighted the importance of developing high-energy-density and high-power-density cathode materials.<sup>1,2</sup> While state-of-the-art layered Li (Ni, Mn, Co) O<sub>2</sub> cathodes demonstrate good power and energy density, there are limitations to potential further enhancements.<sup>3</sup> Moreover, with the vigorous development of the Li-ion industry, millions of tons of Co or Ni will be needed, leading to considerable pressure on metal resources.<sup>4-7</sup> Li-rich cation-disordered rocksalt (DRX) has garnered significant attention owing to its high accessible capacity, which leverages both the cationic redox processes through transition metals (TMs) and the anionic redox processes from lattice oxygen (O).<sup>8</sup> In addition, DRX offers a much broader compositional space, encompassing 4d-6d TM elements such as Ti, V, Cr, Mn, Fe, Co, Ni, Zr, Nb, Mo, Ru, Ta, and W. Notably, utilizing low-cost and earth-abundant elements like Mn, Fe, and Ti presents a promising chance for developing resource-sustainable cathodes. These factors make DRX a promising candidate for the advancement of next-generation cathodes. However, a serious drawback hampers the practical application of DRX: sluggish kinetics, leading to poor rate performances.<sup>9-11</sup>

It is well-accepted that the sluggish kinetic behavior of DRX is attributed to the Li diffusion mechanism.<sup>12-15</sup> In DRX, all cations are randomly distributed over the 4a Wyckoff position, and the anions are in the 4b Wyckoff position, forming

ABCABC sequences in the face-centered cubic sublattice (Figure 1a).<sup>16</sup> The Li diffusion mechanism in the short range can be described as the octahedral-tetrahedral-octahedral (o-t-o) diffusion model, where Li diffuses through hopping from one octahedral site to the next octahedral site via an intermediate tetrahedral site. The diffusion barrier depends on the number of TMs in the octahedron that face-share with the intermediate tetrahedral site, leaving only the 0/1-TM channels with low diffusion barriers. In contrast, the 2/3/4-TM channels experience significant hindrance due to the presence of TMs in adjacent octahedrons (Figure 1b).<sup>17,18</sup> Furthermore, long-range Li percolation in DRX relies on the effective connectivity of the 0/1-TM channels (Figure 1c).<sup>8,19</sup> Unfortunately, the number of 0/1-TM channels is limited, making it difficult to establish effective connections, which restrict Li diffusion kinetics. Increasing the Li content and reducing the short-range order (SRO) of TM can create more 0/1-TM channels.<sup>20-22</sup> However, higher Li content increases material costs and decreases the amount of redox-active TM. Achieving precise control over atomic sites to completely

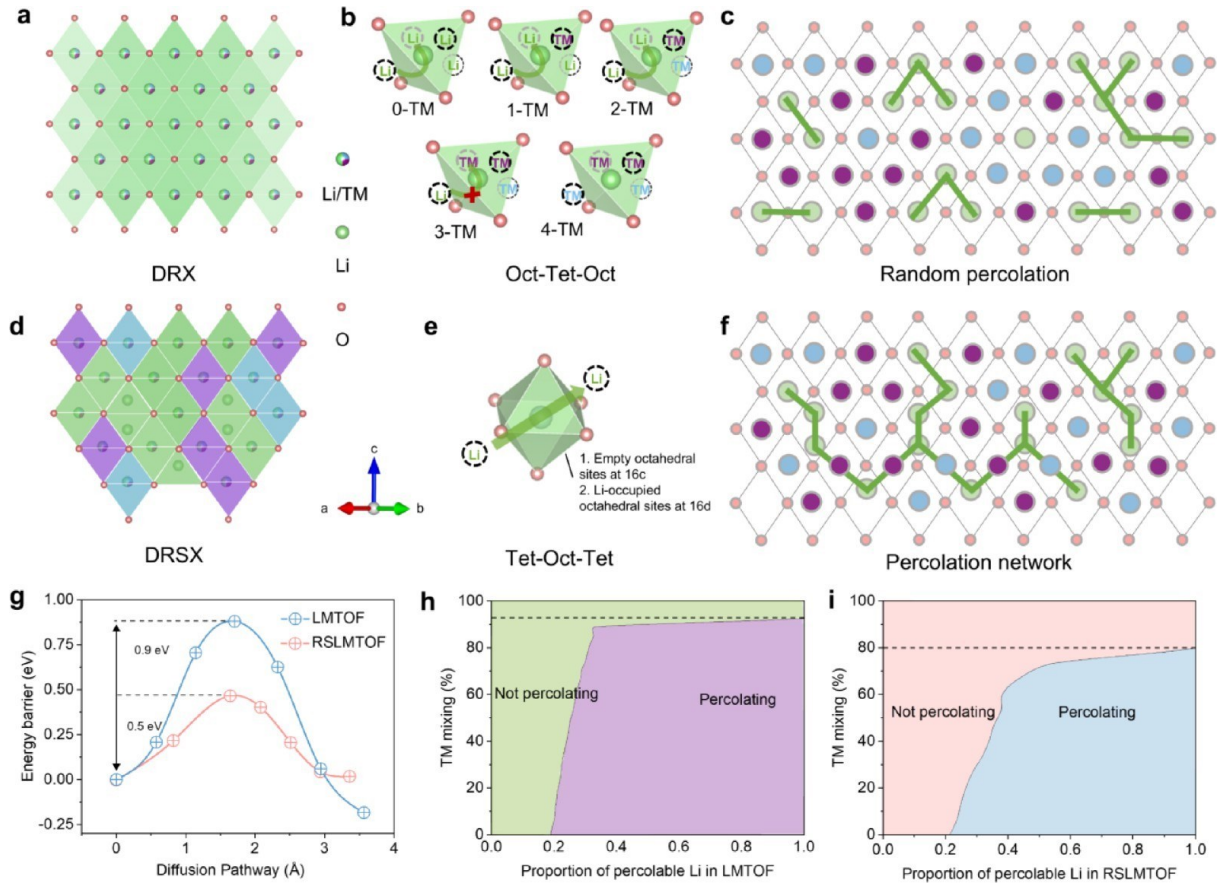


Figure 1. Lithium transport mechanisms in the short range and long range. (a) Illustration of the DRX structure. (b) 0/1/2/3/4-TM diffusion channel in DRX. (c) Illustration of the lithium percolation mechanism. (d) Illustration of the DRSX structure. (e) t-o-t diffusion channel in DRSX. (f) Well-connected percolation network in DRSX. (g) The diffusion energy barrier for LMTOF and RSLMTOF. The impact of TM mixing on Li percolating for LMTOF (h) and RSLMTOF (i).

suppress SRO is also practically challenging. As a result, while DRX offers the potential for high capacity and low cost, its Li diffusion mechanism remains a limiting factor because high-rate Li diffusion cannot be achieved by relying solely on 0/1-TM channels.

In this study, we show that the kinetics of DRX is remarkably improved by injecting a novel tetrahedron-octahedron-tetrahedron (t-o-t) diffusion path through tetrahedral Li stuffing. This strategy begins with a DRX compositing of cost-effective and earth-abundant Mn and Ti elements, which then allows partial Li to migrate from octahedral sites to tetrahedral sites under thermodynamic equilibrium, forming a unique disordered rocksalt/disordered spinel (DRSX) phase structure. A linear correlation between the spinel content and the cationic vacancy concentration is demonstrated, and a continuously linearly adjustable ratio between the two phases is obtained. Benefiting from the additional t-o-t path, the reduction of Li migration barriers and the well-connected Li percolation network improve the Li diffusion kinetics. After that, a high capacity of  $292 \text{ mAh g}^{-1}$  ( $866 \text{ Wh kg}^{-1}$ ) is achieved, which is significantly higher compared to  $157 \text{ mAh g}^{-1}$  ( $483 \text{ Wh kg}^{-1}$ ) of the conventional DRX. As analyzed by the charge compensation mechanism, the high capacity is attributed to extra anionic redox reactions at low voltages and multielectron transfer reactions of Mn. Remarkably, the irreversible release of lattice oxygen and cationic migration are effectively suppressed, thereby preventing structural

densification and ensuring the stability of the Li migration network. Finally, to verify the expandability of this strategy, Mn-rich DRSX materials are developed, showing high capacity ( $311 \text{ mAh g}^{-1}$ ,  $923 \text{ Wh kg}^{-1}$ ) and high rate capacity ( $251 \text{ mAh g}^{-1}$ ,  $697 \text{ Wh kg}^{-1}$  at  $1000 \text{ mA g}^{-1}$ ).

## 2. RESULTS AND DISCUSSION

### 2.1. Tetrahedral Lithium Stuffing Mechanism and Structural Analyses.

Here, we propose improving the kinetic hysteresis of the rocksalt framework materials by increasing the tetrahedral Li occupancy. As shown in Figure 1d, tetrahedral Li stuffing will affect the local structure to form an interwoven structure of disordered rocksalt and disordered spinel (DRSX), whereas spinel-environment components exhibit specific cation distributions, forming high-rate t-o-t diffusion channels (Figure 1e).<sup>23–25</sup> In terms of long-range percolation, tetrahedral Li acts as a low-energy-barrier hub to facilitate a well-connected Li percolation network (Figure 1f). First, to validate the thermodynamic feasibility of DRSX phase formation,  $\text{Li}_{1.25}\text{Mn}_{0.45}\text{Ti}_{0.3}\text{O}_{1.8}\text{F}_{0.2}$  (denoted as LMTOF) was adopted as the model material. First-principles calculation and the special quasi-random structures (SQS) method were carried out with an approximate chemical composition due to limitations in the model size (Figure S1). The spinel phase formation energy diagram shows that when the Li content in LMTOF decreases to around 0.8, the formation of the spinel phase is thermodynamically feasible (Figure S2). Thus, by

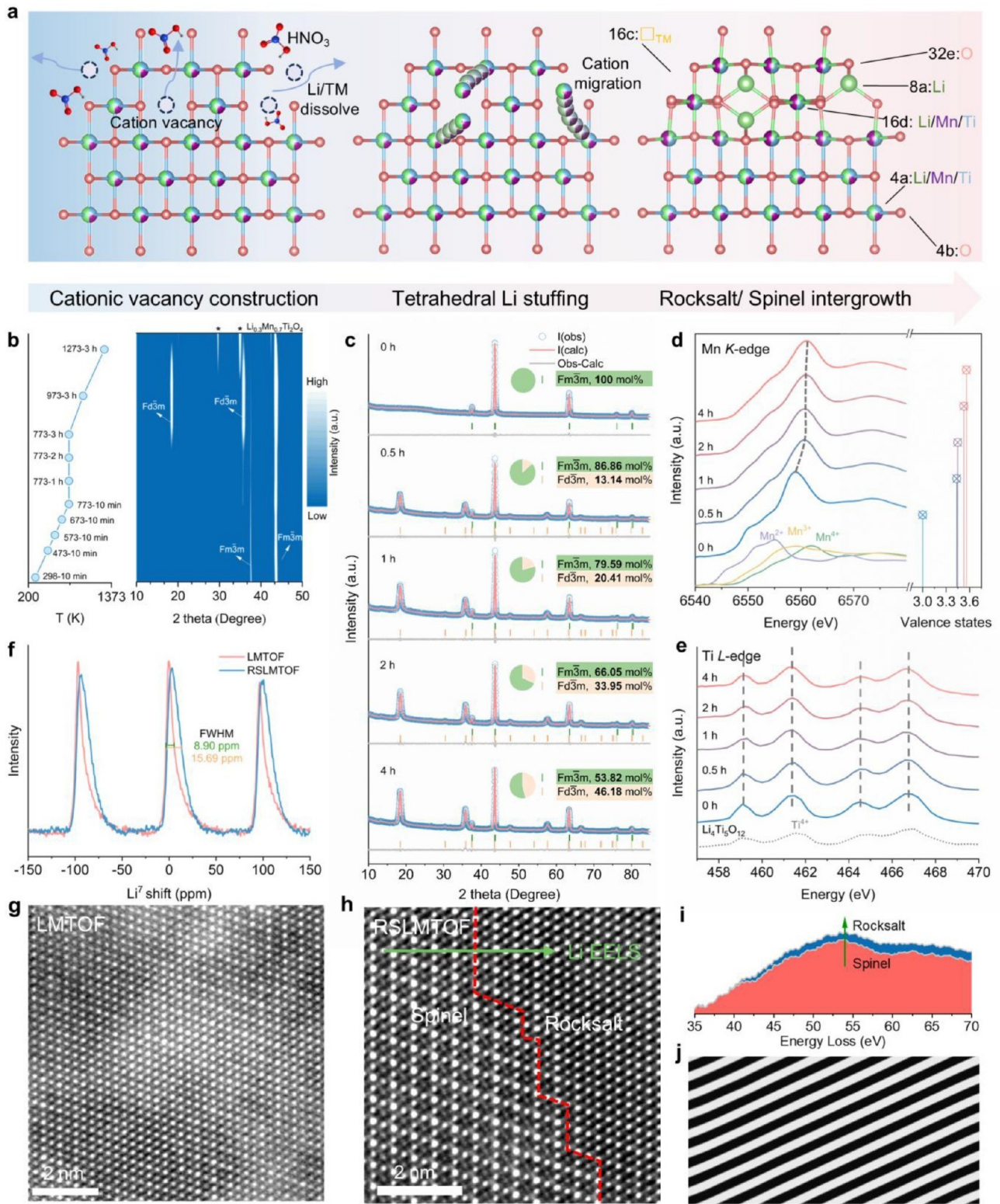


Figure 2. Tetrahedral lithium stuffing process and structural analyses. (a) Illustration of the tetrahedral lithium stuffing process. (b) Ex-situ high-temperature XRD monitoring. (c) Rietveld refinement patterns of XRD for the series of RSLMTOF compounds. (d) XANES and linear combination fitting at the Mn K-edge for LMTOF and RSLMTOF. (e) XANES of LMTOF and RSLMTOF at the Ti L-edge. (f)  $^7\text{Li}$  ssNMR of LMTOF and RSLMTOF. HAADF-STEM images of LMTOF (g) and RSLMTOF (h). (i) EELS of the Li K-edge extracted from Figure 2h. (j) Inverse Fourier transformation pattern at the grain boundary of the RSLMTOF.

carefully controlling the local Li content, tetrahedral lithium can be accommodated, leading to the formation of a DRXS phase structure ( $\text{Li}_{1.25-x}\text{Mn}_{0.45}\text{Ti}_{0.3}\text{O}_{1.8}\text{F}_{0.2}$ , denoted as the

RSLMTOF). Constructing a DRXS material with a Li content of 0.8, where the ratio of DRX phase to spinel phase is 4:3 (Figure S3) and comparing the changes in the diffusion energy

barrier of the o-t-o diffusion channel, the results show that the diffusion energy barrier decreases from 0.9 to 0.5 eV (Figure 1g). It indicates that the o-t-o diffusion channel is more favorable for high-rate Li transport. Figure 1h, i demonstrates the relationship between the occurrence of long-range Li percolation and the degree of TM mixing. It can be concluded that in RSLMTOF, the long-range percolation diffusion of Li ions is no longer heavily dependent on high cation disorder. This indicates that even with a certain degree of disorder, RSLMTOF can achieve efficient Li ion diffusion through a well-connected percolation network.

In practice, LMTOF was prepared via a solid-state method, and RSLMTOF was obtained through tetrahedral lithium stuffing utilizing LMTOF as the raw material. As depicted in Figure 2a, this process can be categorized into three stages: cationic vacancy construction, tetrahedral Li stuffing, and rocksalt/spinel intergrowth. First, to construct cationic vacancies, a chemical leaching method was employed for extracting cationic ions with nitric acid.<sup>26</sup> The elemental compositions of leachable are analyzed by inductively coupled plasma optical emission spectrometry (ICP-OES), as illustrated in Figure S4, showing that the leaching amount of Li, Mn, and Ti is increased with the leaching time and Li leaching content is much higher than Mn/Ti due to lower Li–O bonding energy. During this process, Mn<sup>3+</sup> is partially oxidized to Mn<sup>4+</sup> to maintain charge balance, and the rocksalt structure remains (Figure S5). Subsequently, tetrahedral lithium stuffing was successfully achieved through tempering, and this progress was also monitored using ex-situ X-ray diffraction (XRD). As depicted in Figure 2b, tetrahedral lithium stuffing must meet the thermodynamic conditions (773–973 K) and the kinetic conditions ( $\geq 3$  h). Interestingly, compounds with different leaching times show different phase compositions under the same tempering condition (773 K, 3 h). Rietveld refinement patterns of XRD (Figure 2c) and the corresponding calculated results (Tables S1–S5) validate that between 0 and 4 h of leaching, the  $Fm\bar{3}m$  phase content is decreased from 100 to 53.82 mol % and the  $Fd\bar{3}m$  phase content is increased from 0 to 46.18 mol %, correspondingly. It is found that the  $Fd\bar{3}m$  phase content exhibits a linear relationship with the total concentration of leached cations (Figure S6). Thus, tetrahedral Li occupancy can be continuously manipulated by regulating the cation vacancy content. ICP-OES test results indicate that the chemical composition of the final DRX cathode varies depending on the leaching duration (Table S6). Meanwhile, synchrotron X-ray absorption spectroscopy (XAS) measurements were carried out to probe the chemical state of TM. Figure 2d,e displays the X-ray absorption near-edge structure spectra (XANES) of LMTOF and RSLMTOF with different leaching times at the Mn *K*-edge and Ti *L*-edge. Linear combination fitting results demonstrate that the valence of Mn is increased from +3.00 to +3.56 (Table S7), while no evidence for a change in the oxidation state of Ti is found. After tetrahedral Li stuffing, the coordination environments of Li, Mn, and Ti change, resulting in rocksalt/spinel intergrowth. As shown in Figure 2f, the Li site energy distribution in the RSLMTOF becomes wider, which is confirmed by <sup>7</sup>Li solid-state nuclear magnetic resonance spectroscopy (<sup>7</sup>Li ssNMR). In the DRX phase, partial Li ions are located in the 8a site, forming a LiO<sub>4</sub> tetrahedron, and the others remain a LiO<sub>6</sub> octahedron. This diversification in Li coordination environments results in a broader distribution of Li site energies. To investigate the coordination environment change of Mn and

Ti, the samples were studied by ex-situ extended X-ray absorption fine structure (EXAFS). Fourier transform of the EXAFS data in R space and the corresponding model fitting results of the TM first and second coordination shells are shown in Figures S7 and S8, and Tables S8–S11. For the Mn/Ti–O first coordination shell, a coordination number of 6 is delivered by both LMTOF and RSLMTOF. This suggests that the TM is not filled into the tetrahedral sites as Li. In the case of the second coordination shell for TM–TM, RSLMTOF yields a coordination number of 10 in contrast to 12 in LMTOF. This result verified the presence of a cation vacancy at the 16c site, which confirms the structural characteristics of DRX.

The particle morphology is shown by scanning electron microscopy (SEM), confirming a primary particle size of 1–5  $\mu\text{m}$  for all samples. Elemental mapping depicts the homogeneous distribution of Mn, Ti, O, and F, indicating that no element enrichment occurred after structural reconstruction (Figure S9). It should be noticed that selective peak broadening was applied to  $Fd\bar{3}m$  phase peaks with an odd *l* index when Rietveld refinement was conducted. These peaks, associated with the spinel environment, appear broader than the rocksalt peaks and fit to 12.175–13.370 nm coherence length for the  $Fd\bar{3}m$  phase, considerably smaller than the crystallite size (Figure S10). The structures were further explored by focused ion beam-scanning electron microscopy (FIB-SEM) and scanning transmission electron microscopy (STEM) at the atomic level (Figure S11). Unlike the ordered arrangement of Li and TMs in layered oxide cathodes, bright and dark atoms are observed for LMTOF, proving the disordered arrangement of Li and TMs in DRX (Figure 2g). The extracted line profiles, whereas the *d*-spacing is 2.10 nm, agree well with the feature of the (002) plane in the cubic rocksalt phase with  $a = 4.15$  Å (Figure S12). Figure 2h verifies the DRX phase characteristics of the RSLMTOF. A larger area of the STEM image and locally enlarged domain of two phases are shown, respectively, in Figure S13. The spinel phase and rocksalt phase grow intertwined and are evenly distributed in bulk. The cell parameter of the rocksalt phase is slightly decreased to 4.14 Å, and the cell parameter of the spinel phase is 8.31 Å. As the spinel phase's unit cell size is twice that of the rocksalt phase, it can be speculated that these two intergrown phases are eutectic within one oxygen skeleton. From the spinel phase to the rocksalt phase, electron energy loss spectroscopy (EELS) of the Li *K*-edge reveals an intensified intensity, suggesting the increased Li content in the rocksalt phase (Figure 2i). Fourier transformation and inverse Fourier transformation were performed on the area containing the two-phase interface, and the obtained clear lattice fringes confirm that the two phases are eutectic (Figure 2j). Elemental mapping depicts the homogeneous distribution of Mn, Ti, O, and F throughout the entire sector specimen of LMTOF and RSLMTOF, indicating uniform elemental distribution in the bulk samples (Figure S14).

**2.2. Electrochemical Performances.** The electrochemical behavior of the as-prepared LMTOF and RSLMTOF with different leaching times as cathode materials for Li-ion batteries is investigated utilizing lithium half cells. The results show that the specific capacity, specific energy, and specific power of the cathode materials are greatly improved (Figure S15). RSLMTOF-4h, with the highest tetrahedral occupancy, demonstrated the best rate performance, confirming the effectiveness of the strategy. However, ICP test results reveal

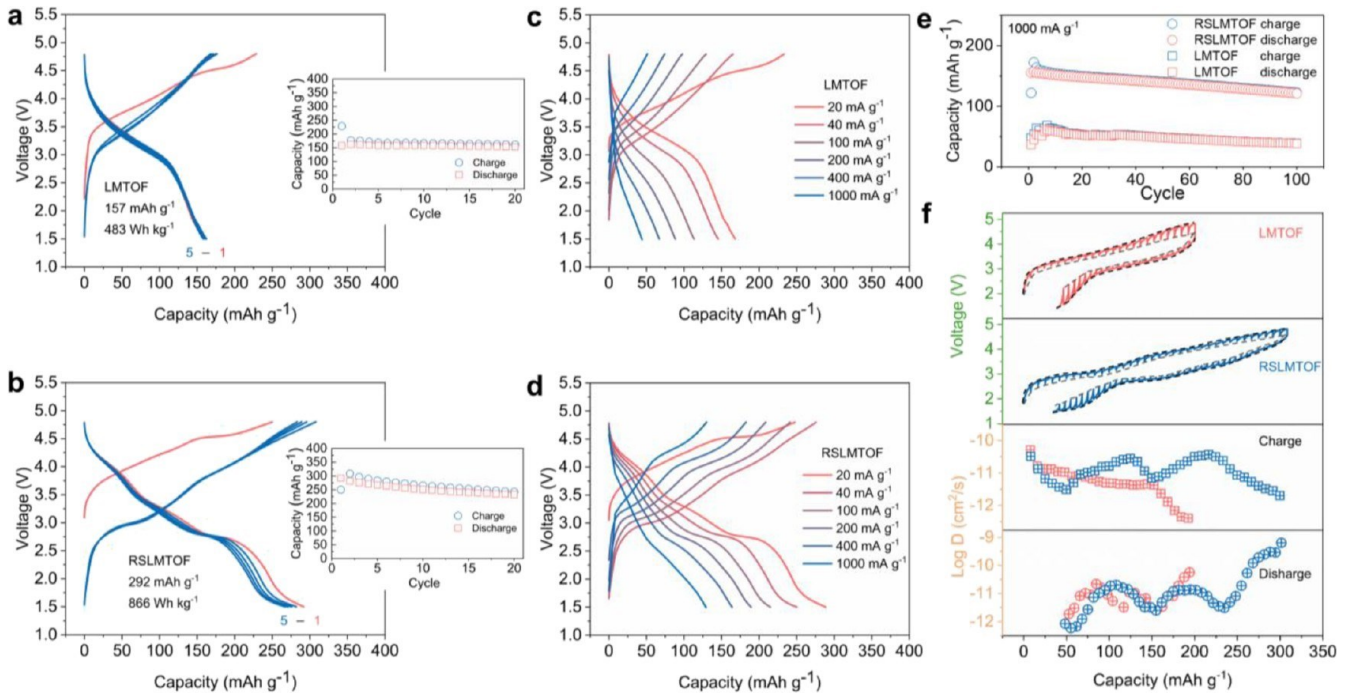


Figure 3. Electrochemical performances of LMTOF and RSLMTOF. Specific capacity voltage curve of the first five cycles for LMTOF (a) and RSLMTOF (b) at a current density of  $20 \text{ mA g}^{-1}$ . The corresponding insets show the cycling performance over 20 cycles. Rate performance for the LMTOF (c) and RSLMTOF (d). (e) Comparison of cycle performance at a current density of  $1000 \text{ mA g}^{-1}$  for LMTOF and RSLMTOF in 100 cycles. (f) GITT curves and Li-ion diffusion coefficient for LMTOF and RSLMTOF.

that the acid-leaching process removes not only Li but also TMs. The loss of redox-active Mn leads to a noticeable decrease in the capacity, particularly at low current densities. Considering both low-rate capacity and high-rate performance, we selected RSLMTOF-1h for subsequent studies. In detail, from Figure 3a,b, it is obvious that the specific discharge capacity and specific energy of RSLMTOF ( $292 \text{ mAh g}^{-1}$ ,  $866 \text{ Wh kg}^{-1}$ ) are significantly higher than those of LMTOF ( $157 \text{ mAh g}^{-1}$ ,  $483 \text{ Wh kg}^{-1}$ ). Note that the first-cycle discharging capacity of RSLMTOF is higher than the charging capacity, suggesting Li reinsertion into 16c cation vacancies. Contrarily, a substantial initial irreversible capacity loss is exhibited by LMTOF. The cycling performance in the insets confirms the more accessible and reversible Li sites of RSLMTOF, resulting from tetrahedral lithium stuffing. To assess the kinetic performance of the reconstructed Li percolation network, the rate capabilities of both cathodes were measured. As shown in Figure 3c,d, for LMTOF, the discharge capacity is decreased to  $44 \text{ mAh g}^{-1}$  at  $1000 \text{ mA g}^{-1}$ . In comparison, the capacity of the RSLMTOF remains at  $129 \text{ mAh g}^{-1}$  at  $1000 \text{ mA g}^{-1}$ . The better rate performance of RSLMTOF is because of the low diffusion energy barrier of the o-t-o diffusion channel and well-connected percolation network. Figure 3e demonstrates the cycling performances of both cathodes at  $1000 \text{ mA g}^{-1}$ . After 100 cycles, the LMTOF was reduced to  $39 \text{ mAh g}^{-1}$ , while the RSLMTOF maintained a value of  $121 \text{ mAh g}^{-1}$ . To further eliminate the kinetic aspects associated with various electronic/atomic motions at different time scales, such as Ohmic resistance (IR drop) and Li diffusion, galvanostatic intermittent titration technique (GITT) tests are performed during the first cycle at  $20 \text{ mA g}^{-1}$  for 25 min of galvanostatic charge/discharge and subsequent relaxation for 2 h. The contrast between the charge/discharge voltage and the relaxation equilibrium voltage (represented by black and gray

dashed lines) indicates the reduced kinetic sluggishness in RSLMTOF. Moreover, the GITT results further reveal that RSLMTOF has a significantly higher lithium-ion diffusion coefficient during the charging process and the initial discharge process (Figure 3f).

**2.3. Redox Mechanism and Structural Evolution.** To uncover the various redox processes participating at different voltages, herein, the samples were studied by ex-situ X-ray absorption near edge spectroscopy (XANES) in the Mn *K*-edge (Figure 4b,c) at states of charge (SoCs) marked in Figure 4a. To check the possible charge compensation of Ti, Ti *K*-edge XANES was performed. According to the position of white-line peaks in Figure 4d and absorption edges in Figure S16, no evidence for a change in the oxidation state of Ti ions is found, indicating that Ti is not responsible for the charge compensation.<sup>27</sup> The results of quantitative analysis for the Mn valence state, obtained through linear combination fitting (Tables S12 and S13), are presented in Figure S17. For LMTOF,  $\text{Mn}^{3+}$  is present in the pristine state and then strongly oxidized to  $+3.92$  when charged from 3.5 to 4.5 V. Continuing the increase in charging voltage to 4.8 V, dominant charge compensation is facilitated through O oxidation. This is confirmed by the O *K*-edge soft X-ray absorption spectroscopy (sXAS) in total electron yield (TEY) mode, where a pre-edge peak at  $\sim 532 \text{ eV}$  (Figure 4e) emerges upon oxidation, corresponding to an electronic transition from O 1s states to the empty O (2p)–Mn (3d) states.<sup>28</sup> Upon discharge to 4.0 V, the valence state of Mn remains unchanged. Instead, the appearance of the pre-edge peak in the O *K*-edge XAS suggests O reduction during the initial stage of discharge. The reduction reaction of  $\text{Mn}^{4+}$  to  $\text{Mn}^{3+}$  occurred from 4.0 to 1.5 V. In the case of RSLMTOF, the first notable feature is the appearance of an additional oxidation peak at 3.2 V. Because Mn is reduced rather than oxidized from 3.60 to 3.46 upon charging

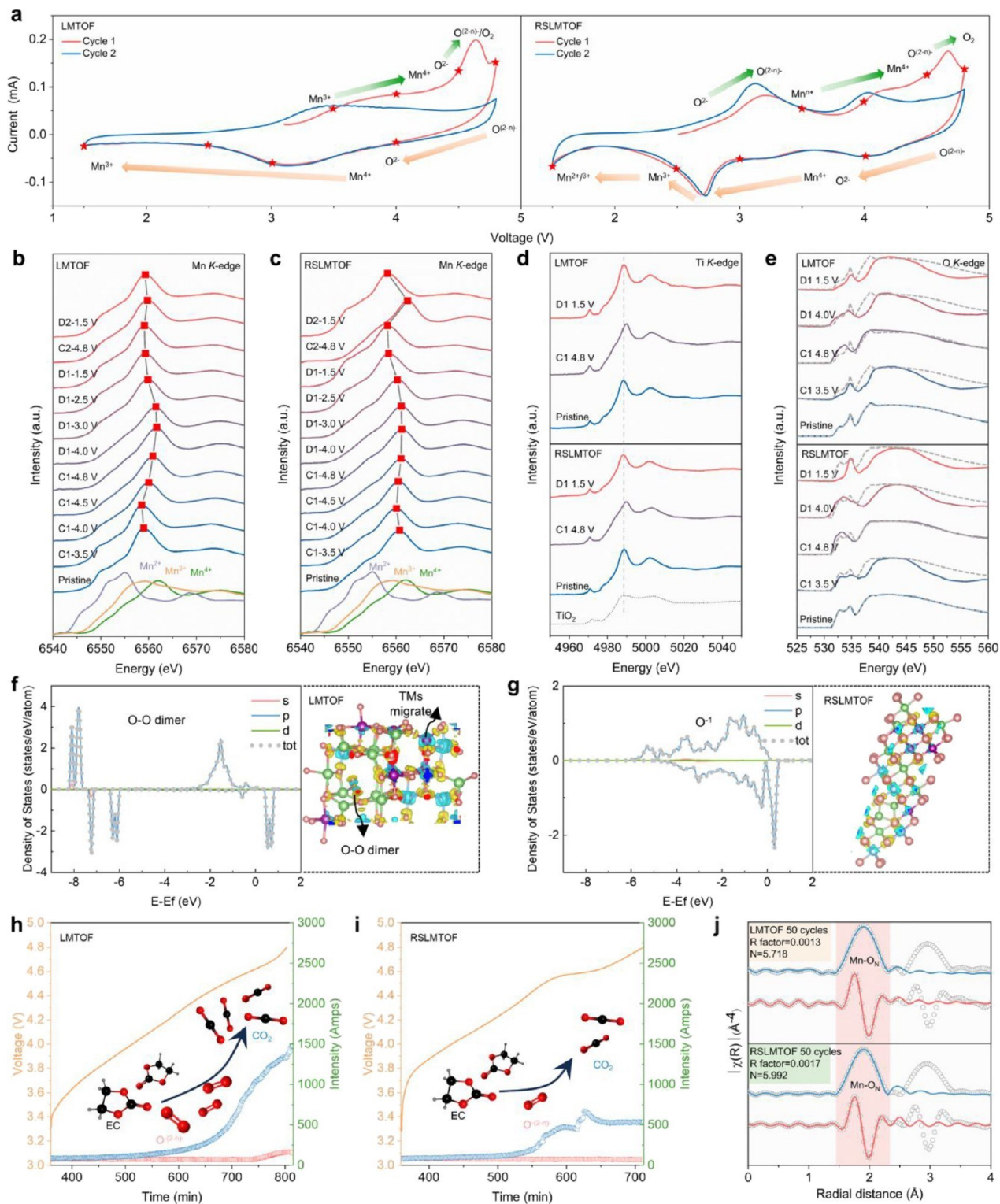


Figure 4. Redox mechanism in LMTOF and RSLMTOF. (a) Cyclic voltammetry profiles for LMTOF and RSLMTOF at voltages from 1.5 to 4.8 V. Ex-situ Mn *K*-edge XANES for LMTOF (b) and RSLMTOF (c) comparing with standards, namely, Mn (Mn<sup>2+</sup>) and Mn<sub>2</sub>O<sub>3</sub> (Mn<sup>3+</sup>) and Li<sub>4</sub>Mn<sub>5</sub>O<sub>12</sub> (Mn<sup>4+</sup>). (d) Ex-situ Ti *K*-edge XANES for LMTOF and RSLMTOF comparing with standards TiO<sub>2</sub> (Ti<sup>4+</sup>). (e) Ex-situ *K*-edge sXAS for LMTOF and RSLMTOF. The O PDOS diagram and corresponding charge difference density map at a charging voltage of 4.6 V for LMTOF (f) and RSLMTOF (g). DEMS results for LMTOF (h) and RSLMTOF (i), showing the evolution of O<sub>2</sub> and CO<sub>2</sub>, together with the galvanostatic charging data. (j) Fourier transform of the EXAFS in R space and the corresponding fitting of the TM first coordination shell of LMTOF and RSLMTOF.

to 3.5 V, the oxidation of O is responsible for the appearance of this low-voltage oxidation peak, as evidenced by the

appearance of the O pre-edge peak. Upon oxidation of O, the Mn–O experiences a ligand-to-metal charge transfer process,

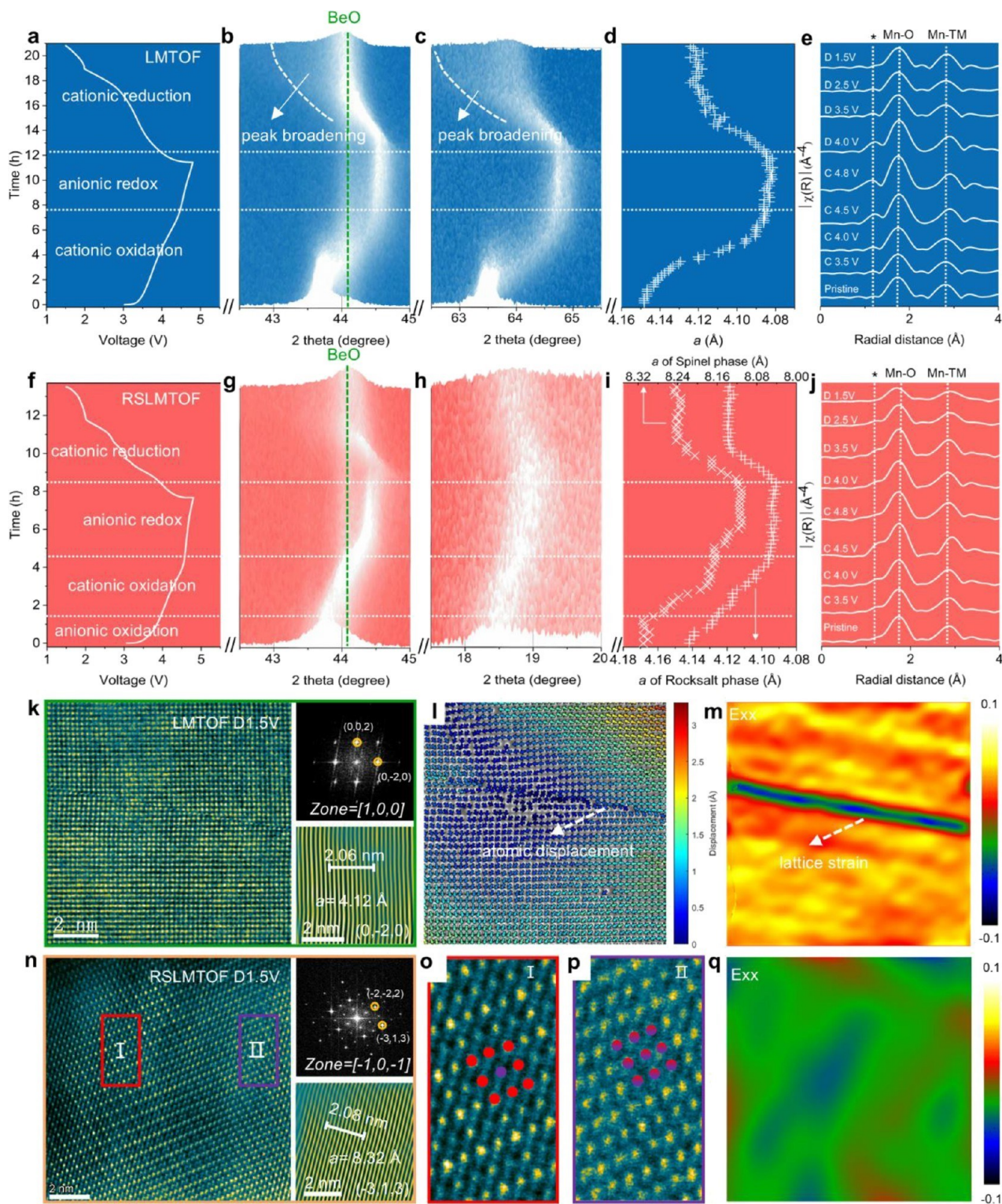


Figure 5. Structural evolution of the LMTOF and RSLMTOF. (a–d) In-situ XRD and corresponding voltage curves and evolution of cell parameter,  $a$  for LMTOF. (e) Fourier transform of the ex-situ EXAFS in R space for the LMTOF. (f–i) In-situ XRD and corresponding voltage curves and evolution of cell parameter,  $a$  for RSLMTOF. (j) Fourier transform of the ex-situ EXAFS in R space for RSLMTOF. (k) HAADF-STEM images, the extracted line profiles, and selected electron diffraction patterns of first-cycled LMTOF at a discharge voltage of 1.5 V. (l) Model-based quantification atomic position of Figure 5k. (m) Lattice strains in Figure 5k analyzed by GPA. (n) HAADF-STEM images, the extracted line profiles, and selected electron diffraction patterns of first-cycled RSLMTOF at the discharge voltage of 1.5 V. The local enlarged domain of rocksalt phase (o) and spinel phase (p). (q) Lattice strains in Figure 5n analyzed by GPA.

resulting in a reduction in the valence state of Mn.<sup>29</sup> This additional low-voltage redox reaction involving oxygen is one

contributing factor to the high capacity observed in RSLMTOF. The second notable feature is the reduction of



Mn to +2.74 at the discharge cutoff voltage, with subsequent complete oxidation to +4 in the second cycle. This reversible multielectron redox reaction of Mn is another reason for the high capacity of RSLMTOF. In contrast, Mn in LMTOF can only be oxidized to +3.22 during the second cycle of charging, which directly leads to reduced capacity. The origin of this phenomenon is likely located in a densification/degradation mechanism because of the irreversible loss of lattice oxygen, as reported by peers.<sup>30</sup> For the LMTOF, lattice oxygen oxidation occurs at high voltages. From the O PDOS diagram, it is directly observed that O–O dimerization produces an O<sub>2</sub> dimer, which leads to irreversible lattice oxygen release, (Figure 4f)<sup>31,32</sup> while the O–O dimerization reaction happens when the voltage exceeds 4.6 V from the charge difference density map, accompanied by TM migration to tetrahedral sites.<sup>33</sup> Interestingly, the electron transfer of lattice oxygen becomes more accessible after tetrahedral lithium stuffing. Because the magnetic characteristics of oxygen directly reflect the charge amount of lattice oxygen, it is observed that the magnetism of lattice oxygen is linearly increased as the Li content decreases, indicating enhanced lattice oxygen activity at low voltages (Figure S18).<sup>34</sup> At high voltages, the O<sub>2</sub> dimers are not reflected by the charge difference density map, showing the improved stability of lattice oxygen. Instead, O–O is demonstrated by the PDOS diagram in Figure 4g. Operando differential electrochemical mass spectroscopy (DEMS) experiments were performed to verify the stability of the oxidized oxygen species toward the release of the O<sub>2</sub> release. The results, presented in Figure 4h,i, show that no gas evolution is initially observed upon oxidation. Significant quantities of O<sub>2</sub> are generated in the form of CO<sub>2</sub> within the cell as electrolyte decomposition is promoted by the O<sub>2</sub> released during operation. This phenomenon becomes particularly pronounced in the LMTOF when the voltage exceeds 4.5 V. Moreover, the accumulation of irreversible lattice oxygen loss continues throughout the cycling process. As shown in Figure 4j, the fitting results for the first coordination number of Mn–O reveal that after 50 cycles, the Mn–O coordination number for LMTOF diminishes to 5.718, whereas RSLMTOF maintains an Mn–O coordination number of 5.992 (Tables S14 and S15). The accumulation of lattice oxygen loss results in the reduction of the Mn valence state and failure of the Li percolation network. This is the underlying cause for the capacity loss observed in the LMTOF.

In-situ XRD analysis was performed to study the structural evolution mechanism. For LMTOF, recalling that the pristine material crystallizes in the cubic space group  $Fm\bar{3}m$  with a single cell parameter,  $a$ , the solid-solution phase transition behavior during cycling is substantiated by an evolute as a function of time (Figure 5a–d). In the cationic oxidation stage, a notable decrease in lattice parameter  $a$  is observed, which subsequently recovers during the cation reduction stage. While, during the anion redox stage, the lattice parameter remains essentially unchanged. It is worth noting that the maximum change in the value of  $a$  is from 4.15 to 4.08 Å, with a change rate of only 1.7%. In contrast to layered structures that experience interlayer repulsion during delithiation, a disordered rock-salt structure avoids this cooperative effect due to random cation occupation. As a result, its lattice variation is primarily sensitive to the Mn–O bond length. Fourier transform of the EXAFS data in R space is shown in Figure 5e. There is no apparent shift in the peak position of the first coordination shell in the R space, which is representative of the

Mn–O bond length. However, a noticeable shoulder peak (marked by “\*”) emerges during the charging process and vanishes during discharging, which suggests that the split Mn–O bond length leads to the distortion of the MnO<sub>6</sub> octahedron.<sup>35</sup> This would bring nanoscale strain with less detectable lattice displacement and is reflected in the broadening of the XRD peaks (Figure 5b,c). Herein, the distortion structure was directly explored by focused ion FIB-SEM (Figure S19) and STEM at the atomic level. As shown in Figure 5k, the atomic resolution electron microscopy image indicates the cubic rocksalt phase with  $a = 4.12$  Å of the first-cycled LMTOF. An efficient approach for accurate and precise model-based quantification of the atomic resolution electron microscopy image was carried out.<sup>36</sup> Following the cycle, there is a clear displacement of atoms from the equilibrium positions in the LMTOF (Figure 5l). These shifts subsequently result in lattice distortion, inducing nanoscale strain (Figure 5m).

During the charge and discharge process, the RSLMTOF also exhibits solid-solution phase transition behavior without the emergence of new phases (Figure 5f–i). The structural evolution mechanisms of the rocksalt phase and spinel phase in RSLMTOF differ due to variations in composition and structure. Specifically, the rocksalt phase in RSLMTOF undergoes a structural evolution process like that of LMTOF, with its maximum change in lattice parameters being from 4.14 to 4.09 Å. The distinction lies in the spinel phase of RSLMTOF, which exhibits essentially unchanged lattice parameters in the initial stage of charge, i.e., the low-voltage oxidation peak region. This indicates that the anionic redox occurring at this stage originates from the spinel phase. The spinel phase lattice parameters exhibit a maximum change from 8.30 to 8.11 Å. Additionally, a comparison of the lattice parameter values between the spinel phase and rocksalt phase in RSLMTOF during the charge and discharge process revealed a consistent ratio close to 2 (Figure S20). This observation implies that the eutectic lattice properties were maintained. Notably, the Mn–O coordination shell in the RSLMTOF does not manifest as a shoulder peak, as observed in the LMTOF (Figure 5j). This suggests that the interwoven structure of the RSLMTOF can effectively mitigate the distortion of MnO<sub>6</sub> during the charge and discharge process and considerably reduce the nanoscale strain. Thus, the XRD peaks remain unchanged. Figure 5n displays the atomic resolution electron microscopy image of cycled RSLMTOF, which shows the rocksalt/spinel interwoven phase with  $a = 8.32$  Å. The interwoven structure is maintained, and the nanoscale strain does not accumulate after cycling (Figure 5o–q). The intergrowth of these two structures offers a promising strategy to mitigate structure distortion during cycling by leveraging structural synergy to enhance stability. However, this approach may inherently limit the phase composition, as maintaining a balance between the two phases is critical to achieving the desired effect. An optimal intergrowth ratio or range may exist that minimizes distortion while preserving high electrochemical performance. Variations in the local composition or distribution of the two phases might lead to inconsistent performance. These warrant further in-depth investigation in future work to achieve optimal performance.

**2.4. Expandability to Mn-Rich Cathodes.** In addition, to explore the influence of Mn and Ti on the formation of the DRX phase, the Mn/Ti ratio was elevated to produce DRX samples with higher Mn content and corresponding lower Ti content, namely, Li<sub>1.2</sub>Mn<sub>0.6</sub>Ti<sub>0.2</sub>O<sub>1.8</sub>F<sub>0.2</sub> (denoted as

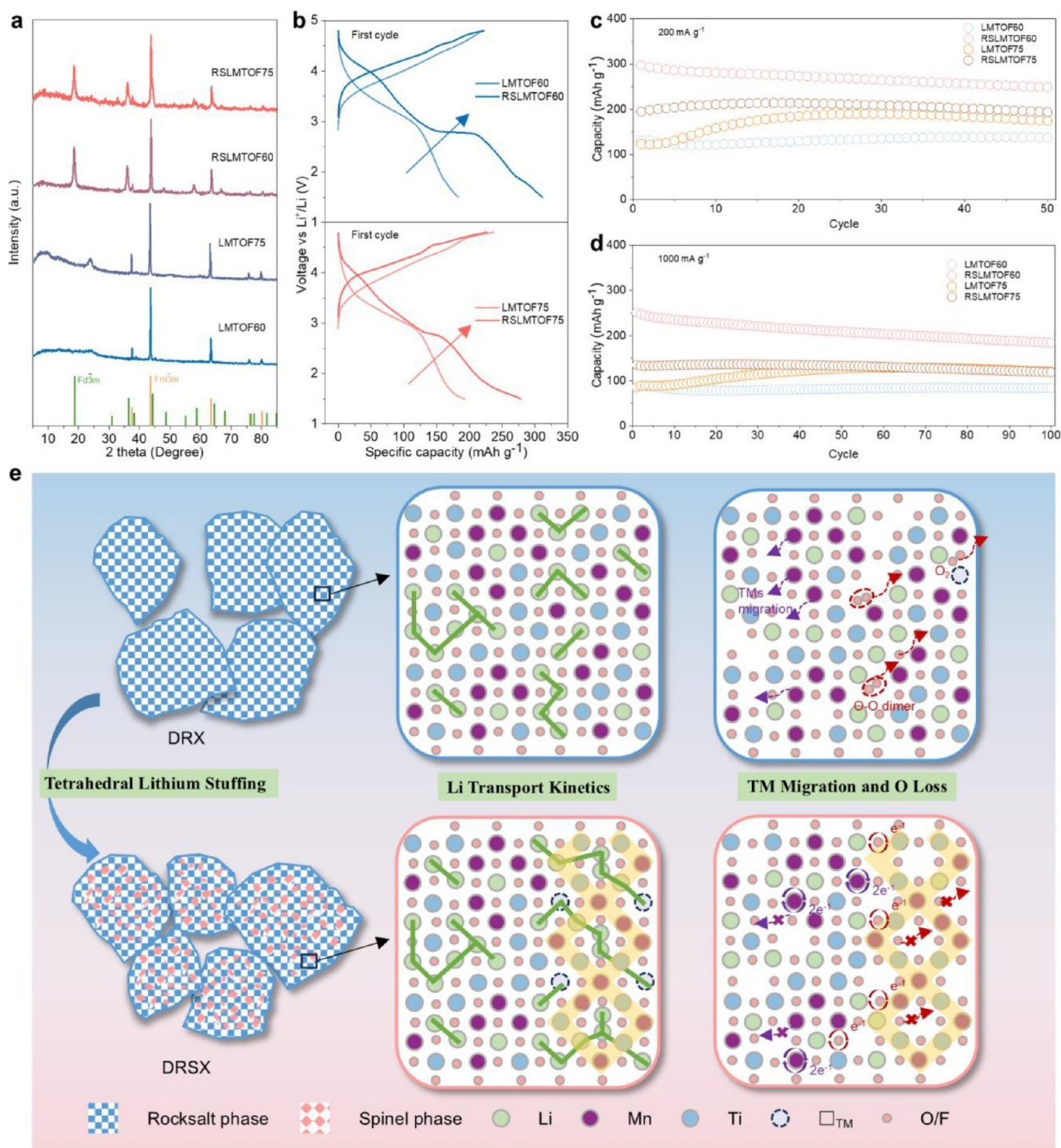


Figure 6. Tetrahedral lithium stuffing in Mn-rich cathodes. (a) XRD patterns of LMTOF60, LMTOF75, RSLMTOF60, and RSLMTOF75. (b) Comparison of the first discharge capacity between LMTOF60 and RSLMTOF60, LMTOF75, and RSLMTOF75. Long-term cycling performance was at current densities of 200 mA g<sup>-1</sup> (c) and 1000 mA g<sup>-1</sup> (d). (e) Schematic diagram of tetrahedral Li stuffing to improve Li transport kinetics and inhibit transition metal migration and oxygen loss in DRX.

LMTOF60) and  $\text{Li}_{1.15}\text{Mn}_{0.75}\text{Ti}_{0.1}\text{O}_{1.8}\text{F}_{0.2}$  (denoted as LMTOF75). DRSX compounds (denoted as RSLMTOF60 and RSLMTOF75) were further obtained through tetrahedral lithium stuffing using LMTOF60 and LMTOF75 as raw materials, respectively. In Figure 6a, XRD reveals that LMTOF60 exhibits a DRX structure, while LMTOF75 exhibits partial SRO rather than a completely DRX structure. It is worth noting that the SRO transforms into a layer-like SRO in RSLMTOF75.<sup>14</sup> Figure 6b demonstrates the effective enhance-

ment of electrochemical performance after structure reconstruction: RSLMTOF60 exhibits a first discharge capacity of 311 mAh g<sup>-1</sup> (923 Wh kg<sup>-1</sup>), compared to LMTOF60 with only 184 mAh g<sup>-1</sup> (552 Wh kg<sup>-1</sup>); RSLMTOF75 shows a capacity of 278 mAh g<sup>-1</sup> (773 Wh kg<sup>-1</sup>), while LMTOF75 demonstrates 192 mAh g<sup>-1</sup> (552 Wh kg<sup>-1</sup>). Figure 6c, d demonstrates the long-term cycling performance at high current densities. The results show that RSLMTOF60 exhibits higher rate capability, displaying a capacity of 297 mAh g<sup>-1</sup>

(84% capacity retention after 50 cycles) at a current density of 200 mA g<sup>-1</sup>, and even at a current density of 1000 mA g<sup>-1</sup>, it maintains a capacity of 251 mAh g<sup>-1</sup> (73% capacity retention after 100 cycles). The capacity increase of LMTOF75 arises from an electrochemical in situ phase transformation.<sup>37</sup> In Figure S21, RSLMTOF60 displays a capacity of 240 mAh g<sup>-1</sup> at a current density of 200 mA g<sup>-1</sup> at 1.5–4.5 V (89.4% capacity retention after 100 cycles). Increasing the Mn content brings more redox-active elements, typically implying higher capacity. However, the decrease in capacity of RSLMTOF75 compared to RSLMTOF60 can be attributed to short-range orders. Maintaining a certain level of Ti content is crucial to sustaining the overall short-range disorder, which is essential in both the DRX and spinel phases. In the spinel phase, Ti elements induce disorder in 16c/16d sites, thereby preventing the collective first-order transition responsible for the 3-V plateau in ordered spinel.<sup>38,39</sup> In DRX, the formation of a disordered structure is impeded by a reduced Ti content. This is due to the properties of d<sup>0</sup> elements, which can endure octahedral distortion resulting from structural disorder with minimal energy cost.<sup>40</sup> Consequently, the capacity to withstand disorder is diminished if the Ti content is decreased, resulting in SRO.

Finally, we present the economic analysis of the RSLMTOF60 cathode (Figure S22). The use of Mn and Ti elements significantly reduces the cost of cathode materials, estimated to be approximately 17% of that of NMC-532 (only considering the TMs). Additionally, RSLMTOF60 exhibits a higher rate capacity compared to other widely studied cathodes, including LiCoO<sub>2</sub>, LiNi<sub>x</sub>Co<sub>y</sub>Mn<sub>z</sub>O<sub>2</sub>, LiFePO<sub>4</sub>, xLi<sub>2</sub>MnO<sub>3</sub>-(1-x)LiMO<sub>2</sub>, and other rocksalt-structured cathodes (Figure S23). Therefore, adopting the strategy of tetrahedral lithium stuffing to develop DRSX materials is indeed of practical significance. Our work is particularly timely given the recent surge of interest in composite-phase structured electrode materials and provides guidance for the good design of structures for cathode materials for high-capacity and high-energy lithium-ion batteries.

### 3. CONCLUSIONS

Overall, we successfully propose a strategy of tetrahedral lithium stuffing, which improves the dynamics of Li-ion transport to address the kinetic sluggishness of the DRX cathode. Tetrahedral Li stuffing affects the local structure to form an interwoven structure of DRSX (Figure 6e). We show that a linear correlation between the spinel phase content and the cationic vacancies is demonstrated and a continuously linearly adjustable ratio between the two phases is achieved. These two phases exhibit intertwined growth characteristics and lattice compatibility. It is worth mentioning that these DRSX materials demonstrate both high-capacity and high-energy characteristics. The enhancement in Li-ion transport dynamics is attributed to the increase in 0-TM channels and the effectiveness of the Li long-range percolation network. Improved charge transfer mainly arises from low-voltage lattice oxygen oxidation and multielectron transfer reactions of Mn, contributing to the high capacity of DRSX materials. Additionally, the enhanced lattice oxygen stability and the suppression of TM migration improve the structural stability, effectively reducing lattice strains and sustaining the effectiveness of Li percolation channels. These findings introduce a Li-site-centered approach to overcoming the kinetic ceiling in DRX materials with sustainable Mn-based electrodes, present-

ing a promising path toward next-generation, high-power, and high-energy lithium-ion batteries. This work highlights the substantial potential for designing high-performance and resource-efficient cathode materials within the expansive framework of rocksalt structures.

### ■ ASSOCIATED CONTENT

#### \*Supporting Information

The Supporting Information is available free of charge at <https://pubs.acs.org/doi/x>

### ■ AUTHOR INFORMATION

#### ■ Corresponding Authors

Tongchao Liu – *Chemical Sciences and Engineering Division, Argonne National Laboratory, Lemont, Illinois 60439, United States*; [orcid.org/0000-0002-6010-3891](https://orcid.org/0000-0002-6010-3891); Email: [liut@anl.gov](mailto:liut@anl.gov)

Xiaobo Ji – *College of Chemistry and Chemical Engineering, Central South University, Changsha 410083, China*; [orcid.org/0000-0002-5405-7913](https://orcid.org/0000-0002-5405-7913); Email: [xji@csu.edu.cn](mailto:xji@csu.edu.cn)

Chaoping Liang – *State Key Laboratory of Powder Metallurgy, Central South University, Changsha 410083, China*; [orcid.org/0000-0002-2910-2938](https://orcid.org/0000-0002-2910-2938); Email: [cpliang@csu.edu.cn](mailto:cpliang@csu.edu.cn)

Khalil Amine – *Chemical Sciences and Engineering Division, Argonne National Laboratory, Lemont, Illinois 60439, United States*; [orcid.org/0000-0001-9206-3719](https://orcid.org/0000-0001-9206-3719); Email: [amine@anl.gov](mailto:amine@anl.gov)

#### ■ Authors

Yu Mei – *College of Chemistry and Chemical Engineering, Central South University, Changsha 410083, China*; *Chemical Sciences and Engineering Division, Argonne National Laboratory, Lemont, Illinois 60439, United States*

Yujin Li – *College of Chemistry and Chemical Engineering, Central South University, Changsha 410083, China*

Haoji Wang – *College of Chemistry and Chemical Engineering, Central South University, Changsha 410083, China*

Jinqiang Gao – *State Key Laboratory of Powder Metallurgy, Central South University, Changsha 410083, China*

Lianshan Ni – *College of Chemistry and Chemical Engineering, Central South University, Changsha 410083, China*

Debbie S. Silvester – *School of Molecular and Life Sciences, Curtin University, Perth, WA 6845, Australia*; [orcid.org/0000-0002-7678-7482](https://orcid.org/0000-0002-7678-7482)

Craig E. Banks – *Faculty of Science and Engineering, Manchester Metropolitan University, Manchester M1 5GD, U.K.*; [orcid.org/0000-0002-0756-9764](https://orcid.org/0000-0002-0756-9764)

Wentao Deng – *College of Chemistry and Chemical Engineering, Central South University, Changsha 410083, China*

Baishan Chen – *Institute for Advanced Study, Central South University, Changsha 410083, China*

Guoqiang Zou – *College of Chemistry and Chemical Engineering, Central South University, Changsha 410083, China*

Hongshuai Hou – College of Chemistry and Chemical Engineering, Central South University, Changsha 410083, China; [orcid.org/0000-0001-8201-4614](https://orcid.org/0000-0001-8201-4614)

Complete contact information is available at:  
<https://pubs.acs.org/10.1021/jacs.4c15631>

### Author Contributions

All authors have given approval to the final version of the manuscript.

### Notes

The authors declare no competing financial interest.

## ACKNOWLEDGMENTS

This work was financially supported by the National Natural Science Foundation of China (52325405, U21A20284, and 52261135632), the Postgraduate Innovation Program of Hunan Province (CX20220201), the Fundamental Research Funds for the Central Universities of Central South University (2023XQLH069), and the Postdoctoral Fellowship Program of CPSF (GZC20242032). We are grateful for technical support from the High-Performance Computing Center of Central South University. This work was also supported by the Clean Vehicles, US-China Clean Energy Research Centre (CERC-CVC2) under the US DOE EERE Vehicle Technologies Office. Argonne National Laboratory is operated for the DOE Office of Science by UChicago Argonne, LLC, under contract number DE-AC02-06CH11357. The authors thank the BL11B and BL14B1 stations in the Shanghai Synchrotron Radiation Facility (SSRF) and the U19 station in the National Synchrotron Radiation Laboratory (NSRL) for XAS measurements.

## REFERENCES

- (1) Li, M.; Lu, J.; Chen, Z. W.; Amine, K. 30 Years of Lithium-Ion Batteries. *Adv. Mater.* 2018, 30 (33), No. 1800561.
- (2) Wu, F. X.; Maier, J.; Yu, Y. Guidelines and trends for next-generation rechargeable lithium and lithium-ion batteries. *Chem. Soc. Rev.* 2020, 49 (5), 1569–1614.
- (3) Zou, K.; Jiang, M.; Ning, T.; Tan, L.; Zheng, J.; Wang, J.; Ji, X.; Li, L. Thermodynamics-directed bulk/grain-boundary engineering for superior electrochemical durability of Ni-rich cathode. *Journal of Energy Chemistry* 2024, 97, 321–331.
- (4) Larcher, D.; Tarascon, J. M. Towards greener and more sustainable batteries for electrical energy storage. *Nat. Chem.* 2015, 7 (1), 19–29.
- (5) Wang, J.; Ji, H.; Li, J.; Liang, Z.; Chen, W.; Zhu, Y.; Ji, G.; Shi, R.; Zhou, G.; Cheng, H.-M. Direct recycling of spent cathode material at ambient conditions via spontaneous lithiation. *Nature Sustainability* 2024, 7 (10), 1283–1293.
- (6) Ji, H.; Wang, J.; Qu, H.; Li, J.; Ji, W.; Qiu, X.; Zhu, Y.; Ren, H.; Shi, R.; Ji, G.; et al. Closed-Loop Direct Upcycling of Spent Ni-Rich Layered Cathodes into High-Voltage Cathode Materials. *Adv. Mater.* 2024, 36 (36), No. e2407029.
- (7) Zheng, N.; Ji, H.; Wang, J.; Zhang, M.; Wei, L.; Shi, R.; Jia, K.; Wu, X.; Xiao, X.; Zhuang, Z.; et al. Surface Catalytic Repair for the Efficient Regeneration of Spent Layered Oxide Cathodes. *J. Am. Chem. Soc.* 2024, 146 (40), 27819–27829.
- (8) Lee, J.; Urban, A.; Li, X.; Su, D.; Hautier, G.; Ceder, G. Unlocking the Potential of Cation-Disordered Oxides for Rechargeable Lithium Batteries. *Science* 2014, 343 (6170), 519–522.
- (9) Chen, D.; Ahn, J.; Chen, G. An Overview of Cation-Disordered Lithium-Excess Rocksalt Cathodes. *ACS Energy Letters* 2021, 1358–1376.
- (10) Kan, W. H.; Deng, B.; Xu, Y.; Shukla, A. K.; Bo, T.; Zhang, S.; Liu, J.; Pianetta, P.; Wang, B.-T.; Liu, Y.; et al. Understanding the Effect of Local Short-Range Ordering on Lithium Diffusion in Li<sub>1.3</sub>Nb<sub>0.3</sub>Mn<sub>0.4</sub>O<sub>2</sub> Single-Crystal Cathode. *Chem.* 2018, 4 (9), 2108–2123.
- (11) Clément, R. J.; Lun, Z.; Ceder, G. Cation-disordered rocksalt transition metal oxides and oxyfluorides for high energy lithium-ion cathodes. *Energy Environ. Sci.* 2020, 13 (2), 345–373.
- (12) Crafton, M. J.; Yue, Y.; Huang, T.-Y.; Tong, W.; McCloskey, B. D. Anion Reactivity in Cation-Disordered Rocksalt Cathode Materials: The Influence of Fluorine Substitution. *Adv. Energy Mater.* 2020, 10 (35), No. 2001500.
- (13) Kan, W. H.; Wei, C.; Chen, D.; Bo, T.; Wang, B.-T.; Zhang, Y.; Tian, Y.; Lee, J.-S.; Liu, Y.; Chen, G. Evolution of Local Structural Ordering and Chemical Distribution upon Delithiation of a Rock Salt Structured Li<sub>1.3</sub>Ta<sub>0.3</sub>Mn<sub>0.4</sub>O<sub>2</sub> Cathode. *Adv. Funct. Mater.* 2019, 29 (17), No. 1808294.
- (14) Huang, J.; Zhong, P.; Ha, Y.; Kwon, D.-H.; Crafton, M. J.; Tian, Y.; Balasubramanian, M.; McCloskey, B. D.; Yang, W.; Ceder, G. Non-topotactic reactions enable high rate capability in Li-rich cathode materials. *Nature Energy* 2021, 6 (7), 706–714.
- (15) Wang, Y.; Huang, S.; Raji-Adefila, B.; Outka, A.; Wang, J. H.; Chen, D. Unraveling the Nature and Role of Layered Cation Ordering in Cation-Disordered Rock-Salt Cathodes. *J. Am. Chem. Soc.* 2022, 144 (43), 19838–19848.
- (16) Urban, A.; Lee, J.; Ceder, G. The Configurational Space of Rocksalt-Type Oxides for High-Capacity Lithium Battery Electrodes. *Adv. Energy Mater.* 2014, 4 (13), No. 1400478.
- (17) Van der Ven, A.; Bhattacharya, J.; Belak, A. A. Understanding Li Diffusion in Li-Intercalation Compounds. *Acc. Chem. Res.* 2013, 46 (5), 1216–1225.
- (18) Anand, S.; Ouyang, B.; Chen, T.; Ceder, G. Impact of the energy landscape on the ionic transport of disordered rocksalt cathodes. *Phys. Rev. Mater.* 2023, 7 (9), No. 095801.
- (19) Ji, H.; Urban, A.; Kitchaev, D. A.; Kwon, D.-H.; Artrith, N.; Ophus, C.; Huang, W.; Cai, Z.; Shi, T.; Kim, J. C.; et al. Hidden structural and chemical order controls lithium transport in cation-disordered oxides for rechargeable batteries. *Nat. Commun.* 2019, 10, 592.
- (20) Cai, Z. J.; Ji, H. W.; Ha, Y.; Liu, J.; Kwon, D. H.; Zhang, Y. Q.; Urban, A.; Foley, E. E.; Giovine, R.; Kim, H.; et al. Realizing continuous cation order-to-disorder tuning in a class of high-energy spinel-type Li-ion cathodes. *Matter-U.S.* 2021, 4 (12), 3897–3916.
- (21) Cai, Z. J.; Ouyang, B.; Hau, H. M.; Chen, T. A.; Giovine, R.; Koirala, K. P.; Li, L. Z.; Ji, H. W.; Ha, Y.; Sun, Y. Z.; et al. In situ formed partially disordered phases as earth-abundant Mn-rich cathode materials. *Nature Energy* 2024, 9 (1), 27–36.
- (22) Ji, H.; Wu, J.; Cai, Z.; Liu, J.; Kwon, D.-H.; Kim, H.; Urban, A.; Papp, J. K.; Foley, E.; Tian, Y.; et al. Ultrahigh power and energy density in partially ordered lithium-ion cathode materials. *Nature Energy* 2020, 5 (3), 213–221.
- (23) Thackeray, M. M.; Amine, K. LiMn<sub>2</sub>O<sub>4</sub> spinel and substituted cathodes. *Nature Energy* 2021, 6 (5), 566–566.
- (24) Manthiram, A.; Chemelewski, K.; Lee, E.-S. A perspective on the high-voltage LiMn<sub>1.5</sub>Ni<sub>0.5</sub>O<sub>4</sub> spinel cathode for lithium-ion batteries. *Energy Environ. Sci.* 2014, 7 (4), 1339–1350.
- (25) Xiao, W. J.; Xin, C.; Li, S. B.; Jie, J. S.; Gu, Y.; Zheng, J. X.; Pan, F. Insight into fast Li diffusion in Li-excess spinel lithium manganese oxide. *J. Mater. Chem. A* 2018, 6 (21), 9893–9898.
- (26) Jung, J. C. Y.; Sui, P. C.; Zhang, J. J. A review of recycling spent lithium-ion battery cathode materials using hydrometallurgical treatments. *Journal of Energy Storage* 2021, 35, No. 102217.
- (27) Farges, F.; Brown, G. E.; Rehr, J. J. Ti K-edge XANES studies of Ti coordination and disorder in oxide compounds: Comparison between theory and experiment. *Phys. Rev. B* 1997, 56 (4), 1809–1819.
- (28) Suntivich, J.; Hong, W. T.; Lee, Y.-L.; Rondinelli, J. M.; Yang, W.; Goodenough, J. B.; Dabrowski, B.; Freeland, J. W.; Shao-Horn, Y. Estimating Hybridization of Transition Metal and Oxygen States in Perovskites from O K-edge X-ray Absorption Spectroscopy. *J. Phys. Chem. C* 2014, 118 (4), 1856–1863.

- (29) Li, B.; Kumar, K.; Roy, I.; Morozov, A. V.; Emelyanova, O. V.; Zhang, L.; Koc, T.; Belin, S.; Cabana, J.; Dedryvere, R.; et al. Capturing dynamic ligand-to-metal charge transfer with a long-lived cationic intermediate for anionic redox. *Nat. Mater.* 2022, 21 (10), 1165.
- (30) Chen, D. C.; Kan, W. H.; Chen, G. Y. Understanding Performance Degradation in Cation-Disordered Rock-Salt Oxide Cathodes. *Adv. Energy Mater.* 2019, 9 (31), 15.
- (31) Ning, F. H.; Li, B.; Song, J.; Zuo, Y. X.; Shang, H. F.; Zhao, Z. M.; Yu, Z.; Chu, W. S.; Zhang, K.; Feng, G.; et al. Inhibition of oxygen dimerization by local symmetry tuning in Li-rich layered oxides for improved stability. *Nat. Commun.* 2020, 11 (1), 4973.
- (32) Tsuchimoto, A.; Shi, X.-M.; Kawai, K.; Mortemard de Boisse, B.; Kikkawa, J.; Asakura, D.; Okubo, M.; Yamada, A. Nonpolarizing oxygen-redox capacity without O-O dimerization in Na<sub>2</sub>Mn<sub>3</sub>O<sub>7</sub>. *Nat. Commun.* 2021, 12 (1), 631.
- (33) McColl, K.; House, R. A.; Rees, G. J.; Squires, A. G.; Coles, S. W.; Bruce, P. G.; Morgan, B. J.; Islam, M. S. Transition metal migration and O<sub>2</sub> formation underpin voltage hysteresis in oxygen-redox disordered rocksalt cathodes. *Nat. Commun.* 2022, 13 (1), 5275.
- (34) Freiman, Y. A.; Jodl, H. J. Solid oxygen. *Phys. Rep.* 2004, 401 (1-4), 1-228.
- (35) Shibata, T.; Bunker, B. A.; Mitchell, J. F. Local distortion of MnO<sub>6</sub> clusters in the metallic phase of La<sub>1-x</sub>Sr<sub>x</sub>MnO<sub>3</sub>. *Phys. Rev. B* 2003, 68 (2), No. 024103.
- (36) De Backer, A.; van den Bos, K. H. W.; Van den Broek, W.; Sijbers, J.; Van Aert, S. StatSTEM: An efficient approach for accurate and precise model-based quantification of atomic resolution electron microscopy images. *Ultramicroscopy* 2016, 171, 104-116.
- (37) Cai, Z.; Ouyang, B.; Hau, H.-M.; Chen, T.; Giovine, R.; Koirala, K. P.; Li, L.; Ji, H.; Ha, Y.; Sun, Y.; et al. In situ formed partially disordered phases as earth-abundant Mn-rich cathode materials. *Nature Energy* 2024, 9 (1), 27-36.
- (38) Chen, T. N.; Yang, J. L.; Barroso-Luque, L.; Ceder, G. Removing the Two-Phase Transition in Spinel LiMn<sub>2</sub>O<sub>4</sub> through Cation Disorder. *Acs Energy Letters* 2023, 8 (1), 314-319.
- (39) Murphy, D. T.; Schmid, S.; Hester, J. R.; Blanchard, P. E. R.; Müller, W. Coordination Site Disorder in Spinel-Type LiMnTiO<sub>4</sub>. *Inorg. Chem.* 2015, 54 (10), 4636-4643.
- (40) Urban, A.; Abdellahi, A.; Dacek, S.; Artrith, N.; Ceder, G. Electronic-Structure Origin of Cation Disorder in Transition-Metal Oxides. *Phys. Rev. Lett.* 2017, 119 (17), No. 176402.